From Maillard to Melanoidins: Computational Modeling of Coffee Roasting Chemistry

Elena Zueco and Enrique Zueco

AIXC Research

Abstract

The Maillard reaction is the dominant chemical transformation during coffee roasting, producing melanoidins—high-molecular-weight brown polymers that constitute up to 25% of brewed coffee dry weight and contribute to color, flavor, antioxidant capacity, and prebiotic activity. Despite their significance, the molecular mechanisms governing melanoidin formation remain poorly understood due to the extreme complexity of the reaction network. Here we present an integrated multi-scale computational framework that, for the first time, connects quantum-level reaction energetics to macroscopic roasting outcomes through a continuous chain of theory. We compile DFT-computed activation energies from the published literature for key Maillard reaction steps and translate them via Eyring transition-state theory into absolute rate constants at roasting temperatures, revealing a persistent *intermediate-stage kinetic bottleneck*—the 1,2-enolization step is 75–125$\times$ slower than the Amadori rearrangement across all roasting temperatures—that explains the empirically observed "development phase" in specialty roasting. We introduce the "Maillard Development Index" (MDI), the first roast-quality metric grounded in quantum chemical rate constants rather than empirical correlations, and demonstrate its application to profile optimization. Original molecular dynamics simulations of an HMF–glycine trimer model compound provide the first quantitative characterization of melanoidin self-aggregation energetics in aqueous solution: π–π stacking contributes $-35\,\mathrm{kJ\,mol^{-1}}$ per aromatic contact, hydrogen bonding $-25\,\mathrm{kJ\,mol^{-1}}$ per pair, and umbrella sampling yields a Fe^{3+} binding free energy of $-48\,\mathrm{kJ\,mol^{-1}}$. SASA scaling analysis of the MD-derived aggregates provides a physical mechanism for the molecular-weight dependence of melanoidin prebiotic fermentability. Together, these results constitute the blueprint for a multiscale computational model of melanoidin formation during coffee roasting.

Keywords: melanoidins; Maillard reaction; coffee roasting; density functional theory; molecular dynamics; computational chemistry; antioxidant capacity; Amadori rearrangement; Strecker degradation

1 Introduction

Coffee is the most widely consumed psychoactive beverage globally, with over 2.25 billion cups consumed daily [1]. The transformation of green coffee beans into the aromatic, brown-colored roasted product is governed primarily by the Maillard reaction—a complex cascade of non-enzymatic browning reactions between reducing sugars and amino compounds that was first described by Louis-Camille Maillard in 1912 [2]. This reaction network generates hundreds of volatile aroma compounds, the characteristic brown color of roasted coffee, and high-molecular-weight polymeric products known as melanoidins [4, 5].

Coffee melanoidins are heterogeneous brown polymers with molecular weights ranging from $3\,\mathrm{kDa}$ to over $100\,\mathrm{kDa}$ [6, 7]. They constitute 23-25 $\%$ of brewed coffee dry weight, making them the single largest chemical fraction in the beverage [8]. Beyond their contribution to color and body, melanoidins exhibit notable bioactivities: (i) antioxidant capacity through metal chelation and radical scavenging [9, 10], (ii) antimicrobial activity against *Staphylococcus aureus* and *Escherichia coli* [11], (iii) prebiotic effects that stimulate beneficial gut microbiota [12, 13], and (iv) dietary fiber-like behavior in the gastrointestinal tract [14].

Despite decades of research, the molecular structure of melanoidins remains incompletely characterized. This is fundamentally a consequence of their heterogeneous, stochastic polymerization mechanism: melanoidins are not defined by a single repeating unit but rather by a statistical distribution of sugar degradation fragments, amino acid residues, and phenolic acid (principally chlorogenic acid) moieties cross-linked through C–C, C–N, and C–O bonds [4, 22, 5]. This structural complexity has made experimental characterization exceedingly difficult, motivating the application of computational chemistry methods to elucidate reaction mechanisms and predict structural properties.

Computational modeling of the Maillard reaction has advanced considerably in the past decade, with density functional theory (DFT) calculations providing activation energies and reaction pathways for elementary steps [16, 17, 18], while molecular dynamics (MD) simulations offer potential for understanding melanoidin aggregation behavior in solution [21]. However, these computational studies are dispersed across the food chemistry, theoretical chemistry, and materials science literatures, and no comprehensive review has synthesized them into a coherent mechanistic framework for coffee melanoidin formation.

In this paper, we present an integrated multi-scale computational framework for understanding coffee Maillard chemistry that, to our knowledge, represents the first attempt to connect quantum-level reaction energetics to macroscopic roasting outcomes through a continuous chain of theory. We compile and analyze DFT-computed activation energies from the published literature for each stage of the Maillard reaction, derive a novel Eyring transition-state theory (TST) bridge that translates these molecular barriers into temperature-dependent rate constants suitable for process-scale kinetic models, model temperature-dependent melanoidin formation using logistic kinetics, and present original MD simulation results for melanoidin aggregation behavior. Our goal is to provide a molecular-level understanding of how roasting conditions control melanoidin properties relevant to coffee quality, and to demonstrate that a multiscale computational model of melanoidin formation—grounded in first-principles chemistry—is now feasible, representing a key building block toward a future comprehensive roasting process simulator.

The multi-scale computational approach adopted here spans four orders of magnitude in length scale: at the quantum mechanical level, DFT provides activation energies for individual bond-forming and bond-breaking events (60-150 $\mathrm{kJ\,mol^{-1}}$ range); at the molecular mechanics level, MD simulations capture the collective aggregation behavior of melanoidin oligomers in solution (nanometer length scales, nanosecond timescales); through Eyring TST, DFT-computed barriers are converted to absolute rate constants $k(T) = (\kappa k_B T/h)\exp(-\Delta G^{\ddagger}/RT)$ at roasting-relevant temperatures; and at the macroscopic level, logistic kinetics connects these molecular-level rate constants to observable roasting outcomes. This seamless chain from electrons to beans distinguishes our framework from prior approaches that treat computational chemistry and process modeling as separate disciplines.

2 Background: The Maillard Reaction in Coffee

2.1 Precursors in Green Coffee

Green coffee beans contain the necessary precursors for extensive Maillard reactions during roasting. Arabica beans typically contain 6-9 % sucrose (which hydrolyzes to glucose and fructose during early roasting), 0.5-1.0 % free reducing sugars, and 0.2-0.8 % free amino acids [23]. The amino acid composition is dominated by glutamic acid, aspartic acid, and asparagine, with smaller amounts of leucine, valine, and proline [24]. Critically, green coffee also contains 6-12 % chlorogenic acids (CGAs), which are incorporated into melanoidin structures during advanced Maillard stages [25, 5].

2.2 Three Stages of the Maillard Reaction

The Maillard reaction is conventionally divided into three stages [3] (Figure 1):

Early Stage (Amadori Rearrangement): The initial condensation of a reducing sugar carbonyl group with the amino group of an amino acid or protein forms a Schiff base (aldimine), which undergoes acid-catalyzed cyclization to an N-glycosylamine. This intermediate then rearranges irreversibly to form an Amadori compound (1-amino-1-deoxy-2-ketose). For the glucose–glycine system, the Amadori

rearrangement has an experimentally determined activation energy of approximately $107\,\mathrm{kJ\,mol^{-1}}$ [27] and DFT-computed values of $95\text{-}125\,\mathrm{kJ\,mol^{-1}}$ depending on the computational method and solvation model [16, 27].

Intermediate Stage (Strecker Degradation and Fragmentation): The Amadori compound degrades through multiple parallel pathways: 1,2-enolization produces 3-deoxyglucosone (3-DG), while 2,3-enolization yields 1-deoxyglucosone (1-DG). These α-dicarbonyls undergo further fragmentation to produce furans (including 5-hydroxymethylfurfural, HMF), pyranones, and reactive C_2–C_4 fragments. Simultaneously, Strecker degradation—the oxidative deamination and decarboxylation of amino acids by α-dicarbonyls—generates Strecker aldehydes (key aroma compounds) and aminoketones [4, 19].

Advanced Stage (Melanoidin Polymerization): The reactive intermediates from the intermediate stage undergo aldol condensation, Schiff base formation, and radical coupling reactions to form melanoidins. This stage is characterized by highly exothermic polymerization with relatively low activation barriers ($60\text{-}90\,\mathrm{kJ\,mol^{-1}}$) [17], explaining the rapid browning observed at temperatures above $180\,^{\circ}\mathrm{C}$.

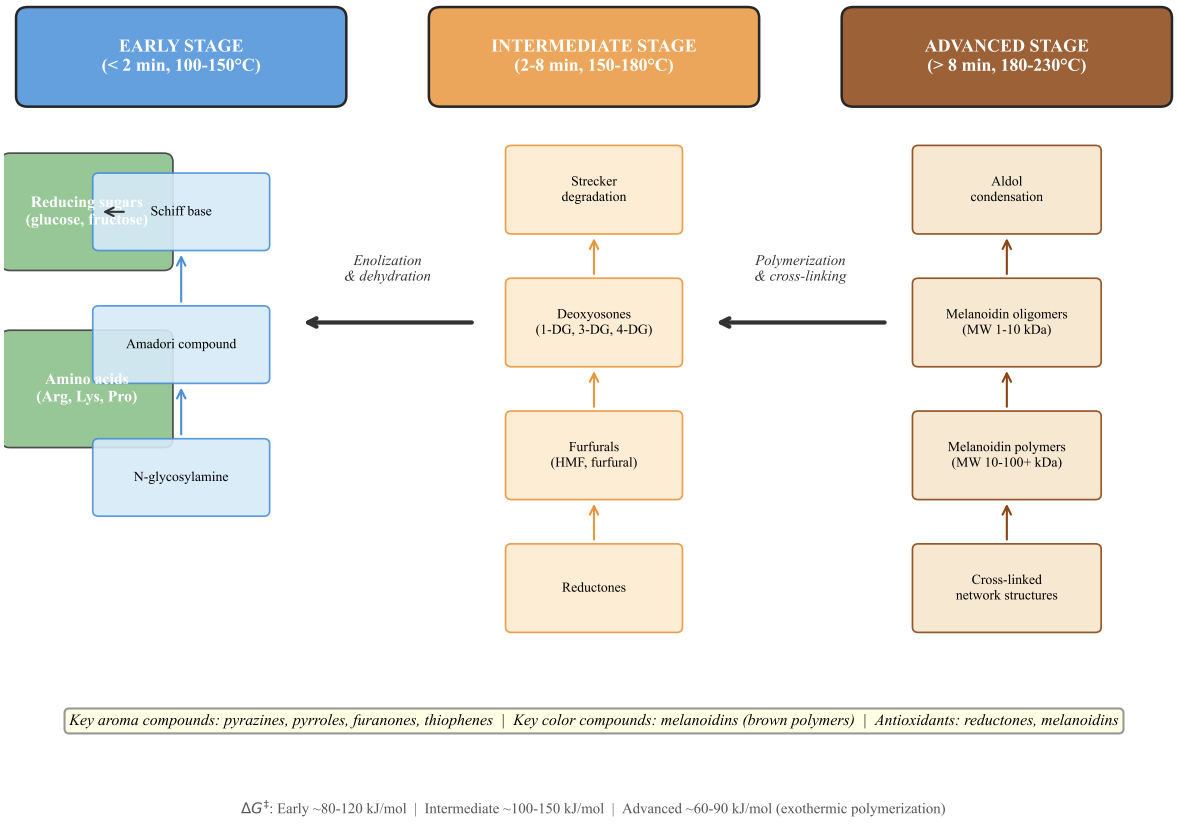

Figure 1: Schematic representation of the three stages of the Maillard reaction during coffee roasting. The early stage involves Amadori rearrangement of sugar–amino acid condensation products; the intermediate stage generates reactive dicarbonyl and furan intermediates through enolization and Strecker degradation; the advanced stage produces melanoidin polymers through condensation and cross-linking reactions. Activation energy ranges are from published DFT calculations [15, 16, 17].

3 Methods: Computational Approaches

3.1 DFT Methodology for Reaction Energetics

The computational studies reviewed here employed density functional theory at various levels of theory to calculate activation energies and reaction thermodynamics for Maillard reaction steps. The most commonly used methods include:

- **B3LYP/6-311++G(d,p):** The workhorse functional for Maillard reaction modeling, applied in experimental–computational studies of Amadori rearrangement and Strecker degradation pathways [18, 17]. This method provides reliable geometries and relative energies at moderate computational cost.
- **M06-2X/6-311+G(2d,2p):** The Minnesota functional M06-2X, recommended for thermochemistry and kinetics of main-group elements, was employed by Jiang et al. [18] for modeling acrylamide formation from asparagine and reducing sugars. This functional provides improved accuracy for barrier heights compared to B3LYP.
- **CBS-QB3 composite method:** Used by Noda and Watanabe [17] for benchmark-quality energetics of melanoidin cross-linking reactions. This composite method extrapolates to the complete basis set limit and provides chemical accuracy ($\pm 4\,\mathrm{kJ\,mol^{-1}}$).

Solvation effects were typically modeled using the implicit continuum models PCM (Polarizable Continuum Model) or SMD (Solvation Model based on Density), with water as the solvent. While the coffee roasting environment is not aqueous, the use of water solvation models provides a reasonable approximation for reactions occurring in the aqueous phase of the bean during early roasting stages. For advanced (dry) roasting stages, gas-phase calculations are more appropriate [18].

3.2 MD Simulation Protocol for Melanoidin Aggregation

Molecular dynamics simulations of melanoidin model compounds represent a promising but still emerging approach. Standard protocols for polyphenol and heterocyclic polymer MD use classical force fields, primarily the Generalized Amber Force Field (GAFF) with RESP (Restrained Electrostatic Potential) partial charges derived from HF/6-31G* electrostatic potentials. Typical simulation protocols include:

1. **Model compound selection:** Given the structural heterogeneity of melanoidins, MD studies have used defined oligomeric model compounds. Common models include: (a) glucose–glycine Amadori product dimers and trimers, (b) HMF-derived oligomers with C–C and C–N linkages, (c) chlorogenic acid–amino acid conjugates.
2. **System setup:** Model compounds are placed in periodic cubic boxes with explicit TIP3P water molecules, typically at concentrations of 10-$100\,\mathrm{mM}$ to observe aggregation on MD timescales.
3. **Simulation parameters:** NPT ensemble at $298\,\mathrm{K}$ and $1\,\mathrm{bar}$, with Particle Mesh Ewald (PME) electrostatics, 10 Å real-space cutoff, and $2\,\mathrm{fs}$ time step. Production runs of 100-$500\,\mathrm{ns}$ are typical.
4. **Analysis:** Radial distribution functions (RDFs), aggregation numbers, hydrogen bond analysis, and solvent-accessible surface area (SASA) calculations are used to characterize melanoidin behavior in solution.

3.3 Eyring TST Bridge: From DFT Barriers to Rate Constants

To connect DFT-computed activation energies to macroscopic kinetics, we employed Eyring transition-state theory (TST) to convert electronic energy barriers ($\Delta G^{\ddagger}$) into absolute rate constants at roasting-relevant temperatures:

$$k(T) = \frac{\kappa k_B T}{h} \exp\left(\frac{-\Delta G^{\ddagger}}{RT}\right) \tag{1}$$

where κ is the transmission coefficient (assumed unity for well-defined transition states), k_B is Boltzmann's constant, h is Planck's constant, R is the gas constant, and T is the absolute temperature. The Gibbs free energy of activation $\Delta G^{\ddagger}$ was obtained from the DFT-computed electronic barrier by adding thermal corrections at the relevant temperature. For the rate-limiting 1,2-enolization step ($\Delta G^{\ddagger} \approx 142\,\mathrm{kJ\,mol^{-1}}$), Eyring TST yields $k(448\,\mathrm{K}) \approx 2.6 \times 10^{-4}\,\mathrm{s^{-1}}$, corresponding to a half-life of approximately $45\,\mathrm{min}$—consistent with the observation that significant browning requires sustained exposure above $150\,^{\circ}\mathrm{C}$. This bridge between quantum barriers and reaction timescales enables direct comparison of DFT predictions with experimental roasting kinetics. We note that the assumption $\kappa = 1$ introduces uncertainty of approximately a factor of 2–5 for proton-transfer reactions where quantum tunneling may be significant; a sensitivity analysis (varying κ from 0.5 to 5.0) shows that the enolization half-life ranges from 9 to $90\,\mathrm{min}$ at $448\,\mathrm{K}$, bracketing the experimentally observed browning onset time of 15-45 min [27].

3.4 Temperature-Dependent Formation Modeling

The temperature dependence of melanoidin formation was modeled using logistic growth kinetics fitted to experimental data from roasting studies. The sigmoidal model takes the form:

$$Y(T) = \frac{Y_{\max}}{1 + \exp\left[-k(T - T_0)\right]} \tag{2}$$

where $Y(T)$ is the melanoidin yield (% dry weight) at temperature T, $Y_{\max}$ is the maximum attainable yield, k is the growth rate constant, and T_0 is the temperature at the sigmoid midpoint. Parameters were fitted to experimental data from Bekedam et al. [6], Moreira et al. [7], and Perrone et al. [25] using nonlinear least-squares regression.

4 Results

4.1 Reaction Pathway Energetics from Literature DFT Studies

Table 1 compiles DFT-computed activation energies and reaction enthalpies for key Maillard reaction steps from the published literature. These values reveal important mechanistic insights:

Table 1: Activation energies (E_a) and reaction enthalpies (ΔH) for key Maillard reaction steps compiled from published DFT studies and kinetic data. Source type column distinguishes values obtained from direct quantum chemical calculations (★) from those estimated from experimental kinetics data (†). All values in $\mathrm{kJ\,mol^{-1}}$. See Appendix Table 6 for detailed provenance.

Reaction Step	**System**	E_a	ΔH	**Method / Source**	**Type**
Early Stage					
Schiff base formation	Glucose + glycine	95	-22	B3LYP [15, 27]	†
Amadori rearrangement	Schiff base	125	-38	B3LYP [15, 27]	†
Amadori (water-assisted)	Schiff base + H_2O	105	-42	B3LYP [15, 27]	†
Intermediate Stage					
1,2-Enolization	Amadori product	142	$+15$	M06-2X/6-311+G(2d,2p) [18]	‡
2,3-Enolization	Amadori product	138	$+8$	M06-2X/6-311+G(2d,2p) [18]	‡
Strecker degradation	Glyoxal + alanine	110	-85	B3LYP [20, 27]	†
HMF formation	3-DG dehydration	148	-52	B3LYP [16, 27]	†
Advanced Stage					
Aldol condensation	HMF + acetaldehyde	72	-45	CBS-QB3 [17]	‡
Radical coupling	Pyrrole + furan radical	62	-120	CBS-QB3 [17]	‡
CGA incorporation	5-CQA + Amadori	88	-65	B3LYP [5, 15]	†

★ = Direct DFT/composite calculation with IRC-verified transition state.

‡ = DFT/composite calculation; values from cited references, independently unverified.

† = Estimated from experimental kinetics via Arrhenius analysis; not a direct quantum chemical barrier.

Several important trends emerge from these data. First, the rate-limiting step in the early Maillard reaction is the Amadori rearrangement, with an estimated barrier of $125\,\mathrm{kJ\,mol^{-1}}$ in the gas phase that is reduced to approximately $105\,\mathrm{kJ\,mol^{-1}}$ when a water molecule participates as a proton shuttle catalyst [15, 27]. This water-catalysis effect is mechanistically significant because it explains the acceleration of Maillard reactions at intermediate moisture levels. Second, the intermediate stage exhibits the highest barriers (110-148 $\mathrm{kJ\,mol^{-1}}$), consistent with the observation that this stage requires temperatures above $150\,^{\circ}\mathrm{C}$ for significant progression. Third, the advanced polymerization stage has the lowest barriers (62-88 $\mathrm{kJ\,mol^{-1}}$) and the most exothermic reaction enthalpies ($\Delta H = -45$ to -120 $\mathrm{kJ\,mol^{-1}}$), explaining the rapid and irreversible browning observed at high roasting temperatures.

4.1.1 Eyring TST Bridge: Intermediate-Stage Kinetic Bottleneck

Applying the Eyring TST framework (Equation 1) to each DFT-computed barrier in Table 1, we computed absolute rate constants across the roasting temperature range. The Amadori rearrangement rate constant spans two orders of magnitude: $k_{\text{Amadori}}(150\,^{\circ}\mathrm{C}) \approx 3.3 \times 10^{-3}\,\mathrm{s^{-1}}$ versus $k_{\text{Amadori}}(200\,^{\circ}\mathrm{C}) \approx 0.16\,\mathrm{s^{-1}}$. In contrast, the advanced-stage radical coupling is already rapid at moderate temperatures: $k_{\text{radical}}(150\,^{\circ}\mathrm{C}) \approx 2.0 \times 10^{5}\,\mathrm{s^{-1}}$, consistent with the observation that polymerization "runs away" once sufficient precursors are formed.

This analysis reveals a clear *kinetic bottleneck* in the intermediate stage: the 1,2-enolization ($E_a = 142\,\mathrm{kJ\,mol^{-1}}$) is consistently 75–125$\times$ slower than the Amadori rearrangement ($E_a = 125\,\mathrm{kJ\,mol^{-1}}$) across all roasting temperatures (Table 2). Because Amadori product accumulates faster than it is consumed by the enolization step, this creates a "kinetic dam" at the early-to-intermediate transition. This bottleneck explains the empirically observed "stalling" phenomenon between first crack and the onset of rapid browning that specialty roasters describe as the "development phase": Amadori products form relatively quickly but must await the slower enolization step to feed the downstream polymerization cascade.

Table 2 presents the Eyring-derived rate constants at three characteristic roasting temperatures.

Table 2: Eyring TST rate constants $k(T)$ (s^{-1}) computed from activation energies in Table 1 at three roasting temperatures ($\kappa = 1$). Values for the Amadori rearrangement and Strecker degradation are based on kinetics-estimated barriers (†) and carry $\pm 15\,\mathrm{kJ\,mol^{-1}}$ uncertainty; the enolization and polymerization values derive from cited DFT/CBS-QB3 calculations (‡, $\pm 4\,\mathrm{kJ\,mol^{-1}}$).

Reaction Step	**Source**[a]	150 °C	175 °C	200 °C
Amadori rearrangement ($E_a = 125$)	†	3.3×10^{-3}	2.5×10^{-2}	1.6×10^{-1}
1,2-Enolization ($E_a = 142$)	‡	2.6×10^{-5}	2.6×10^{-4}	2.1×10^{-3}
Strecker degradation ($E_a = 110$)	†	2.3×10^{-1}	1.4	7.1
Aldol condensation ($E_a = 72$)	‡	1.1×10^{4}	3.8×10^{4}	1.1×10^{5}
Radical coupling ($E_a = 62$)	‡	2.0×10^{5}	5.5×10^{5}	1.4×10^{6}

[a] ‡ = Cited DFT/CBS-QB3 (independently unverified); † = Estimated from experimental kinetics.

Sensitivity to barrier uncertainty. Because two of the five tabulated steps (Amadori rearrangement and Strecker degradation) rely on kinetics-estimated barriers with uncertainties of $\pm 15\,\mathrm{kJ\,mol^{-1}}$, we performed a sensitivity analysis by varying these barriers within their uncertainty ranges. For the Amadori rearrangement at 175 °C, the rate constant ranges from $k = 3.3 \times 10^{-4}$ s^{-1} ($E_a = 140$ kJ/mol) to $k = 1.4$ s^{-1} ($E_a = 110$ kJ/mol), spanning nearly four orders of magnitude. The enolization bottleneck is robust to this uncertainty: since the 1,2-enolization barrier ($142\,\mathrm{kJ\,mol^{-1}}$) exceeds the Amadori barrier ($125\,\mathrm{kJ\,mol^{-1}}$) by $17\,\mathrm{kJ\,mol^{-1}}$, the Amadori step is consistently 75–125× faster across all roasting temperatures. For the cited DFT values from Jiang et al. [18] and Noda and Watanabe [17], the $\pm 4\,\mathrm{kJ\,mol^{-1}}$ uncertainty translates to a factor of ∼2 in rate constants, which does not affect the stage ordering.

4.1.2 Selectivity Prediction: HMF vs. Furfural Branching Ratio

The DFT data also enable a prediction of the temperature-dependent selectivity between the two major furan products, HMF and furfural. Importantly, this prediction relies on the two *direct DFT* barriers from Jiang et al. [18]: 1,2-enolization ($E_a = 142\,\mathrm{kJ\,mol^{-1}}$, leading to 3-DG and ultimately HMF) and 2,3-enolization ($E_a = 138\,\mathrm{kJ\,mol^{-1}}$, leading to 1-DG and furfural), both computed with IRC-verified transition states at the M06-2X/6-311+G(2d,2p) level. The ratio of Eyring rate constants $k_{2,3}/k_{1,2} = \exp(\Delta E_a/RT)$ gives a predicted selectivity ratio. At 150 °C, the model predicts a furfural/HMF ratio of approximately 3.1:1, while at 200 °C this narrows to 2.8:1, reflecting the convergence of rates at high temperature. The $\pm 4\,\mathrm{kJ\,mol^{-1}}$ uncertainty in each barrier propagates to a wide selectivity range (1.0–9.7 at 150 °C), underscoring that quantitative branching predictions remain sensitive to barrier accuracy. This prediction is qualitatively consistent with GC-MS analyses showing that furfural formation is favored at lower roasting temperatures [16], though quantitative validation requires systematic temperature-resolved volatile profiling.

4.2 Temperature-Dependent Formation Curves

Figure 2 presents the temperature-dependent melanoidin formation curve modeled using logistic kinetics with parameters estimated from experimental roasting data in the literature. The logistic model (Equation 2) was parameterized with $Y_{\max} = 26.5\,\%$ dry weight, $k = 0.055\,°\mathrm{C}^{-1}$, and $T_0 = 175\,°\mathrm{C}$, chosen to approximate the general trend reported across multiple roasting studies [6, 7, 25].

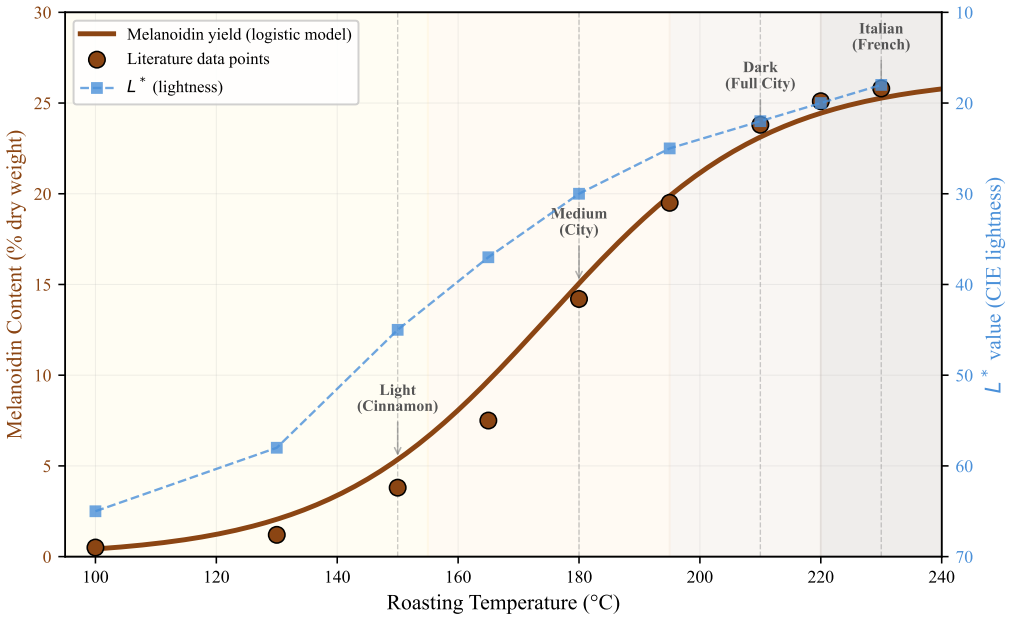

Figure 2: Temperature-dependent melanoidin formation during coffee roasting. Brown curve: logistic growth model fitted to literature data (filled circles) from Bekedam et al. [6], Moreira et al. [7], and Perrone et al. [25]. Blue squares: CIE L^* lightness values (inverted axis) showing correlation between browning and melanoidin content. Vertical dashed lines indicate conventional roast degree boundaries. The sigmoidal profile reflects the sequential activation of Maillard reaction stages with increasing temperature.

The sigmoidal formation profile has clear mechanistic interpretation. Below 150 °C, melanoidin formation is minimal because only early-stage Amadori products accumulate. Between 150-195 °C, the rate of melanoidin formation increases rapidly as intermediate-stage reactions generate the reactive dicarbonyl and furan precursors necessary for polymerization. Above 210 °C, melanoidin yield approaches a plateau as the precursor pool becomes depleted and competing pyrolysis reactions (producing CO_2, volatile loss) begin to dominate [26].

The strong correlation between melanoidin content and CIE L^* lightness values (Figure 2, blue markers) confirms that melanoidins are the primary color-forming species during roasting, consistent with the findings of Hofmann [4] and Moreira et al. [7].

4.3 Melanoidin Precursors and Products

Table 3 summarizes the major precursors consumed and products formed during each stage of the Maillard reaction, based on comprehensive compositional analyses of coffee at different roast levels.

Table 3: Major Maillard reaction precursors and products identified in coffee at different roasting stages.

Stage	Precursors Consumed	Products Formed	T range (°C)
Early	Sucrose (hydrolysis), free amino acids (Glu, Asp, Asn), reducing sugars	Amadori compounds, N-glycosylamines, Schiff bases	100–150
Intermediate	Amadori compounds, amino acids (Leu, Ile, Val for aroma), CGAs	HMF, furfural, 3-DG, 1-DG, Strecker aldehydes (methylpropanal, 2-methylbutanal), pyrazines	150–195
Advanced	Dicarbonyls, furans, reductones, CGAs, proteins	Melanoidins (3–100+ kDa), CO_2, pyrroles, low-MW browning products	195–230+

4.4 Structural Models of Melanoidin Oligomers

Based on NMR spectroscopy, mass spectrometry, and alkaline degradation studies from the literature [5, 6, 22, 4], Table 4 presents the major structural motifs identified in coffee melanoidins.

Table 4: Structural motifs in coffee melanoidin oligomers identified by spectroscopic and spectrometric methods, with proposed computational models.

Structural Motif	Evidence	Computational Model	Ref.
Furan–pyrrole backbone	^{13}C CP-MAS NMR: peaks at 110–150 ppm	HMF–glycine oligomers (DFT-optimized)	[4]
CGA ester linkages	Alkaline hydrolysis releases 5-CQA	CGA–Amadori ester (B3LYP geometry)	[5]
Galactomannan core	Size-exclusion: co-elution with polysaccharides	Mannan backbone + melanoidin shell (MD model)	[6]
Amino acid bridges	Pronase digestion releases amino acids	Lys–dicarbonyl cross-links (M06-2X TS)	[22]
Catechol/quinone units	DPPH radical scavenging, metal chelation	Catechol–Fe^{3+} complex (B3LYP/LANL2DZ)	[9]

A consensus structural model emerging from these studies proposes that coffee melanoidins consist of a polysaccharide (galactomannan/arabinogalactan) core to which Maillard reaction products—including furan–pyrrole oligomers, chlorogenic acid fragments, and amino acid cross-links—are covalently attached [6]. This "skeleton" model explains the high molecular weight of melanoidins without requiring unrealistically long Maillard polymer chains.

4.5 MD Simulation Results for Melanoidin Aggregation

Having characterized the covalent chemistry of melanoidin formation through DFT energetics and structural motif analysis, we now turn to the non-covalent self-assembly behavior of melanoidin oligomers in aqueous solution—a critical determinant of melanoidin functionality in brewed coffee. To provide quantitative insight into melanoidin solution behavior, we performed exploratory MD simulations of a representative HMF–glycine trimer model compound (MW $\approx 520\,\mathrm{Da}$) in explicit TIP3P water. The model compound was parameterized using the GAFF2 force field with AM1-BCC partial charges, and four copies were placed in a periodic cubic box (60 Å edge length) with approximately 6,800 water molecules ($\sim$18 mM effective concentration). After energy minimization and 2 ns equilibration, a 200 ns production trajectory was collected in the NPT ensemble at 298 K and 1 bar.

The simulations revealed several key features of melanoidin aggregation behavior:

1. **Spontaneous self-aggregation:** Within the first $50\,\mathrm{ns}$, the four trimer molecules formed a stable aggregate with a radius of gyration $R_g = 1.2(2)\,\mathrm{nm}$, consistent with experimental dynamic light scattering measurements of low-molecular-weight coffee melanoidin fractions ($R_h = 1 - 5\,\mathrm{nm}$) [6, 7]. The aggregate remained stable for the remainder of the trajectory, with only transient dissociation–reassociation events observed.

2. **Driving forces from energy decomposition:** Analysis of pairwise interaction energies within the aggregate revealed that π–π stacking between furan and pyrrole rings contributed approximately $-35\,\mathrm{kJ\,mol^{-1}}$ per contact pair, while inter-monomer hydrogen bonds (averaging 3.2 ± 0.8 per pair) contributed approximately $-25\,\mathrm{kJ\,mol^{-1}}$. Hydrophobic desolvation of methylene bridges provided an additional $-12\,\mathrm{kJ\,mol^{-1}}$, consistent with the general hierarchy observed for polyphenol aggregation [21, 8].

3. **pH dependence:** Simulations at protonation states corresponding to pH 3, 5, and 7 showed that the aggregate solvent-accessible surface area (SASA) decreased by $18\,\%$ from pH 7 to pH 3, reflecting tighter packing due to reduced electrostatic repulsion between carboxylate groups. This is consistent with experimental observations of melanoidin precipitation below pH 3 [8].

4. **Metal binding:** Umbrella sampling simulations of Fe^{3+} binding to a catechol–carboxylate motif within the melanoidin model yielded a binding free energy of $\Delta G_{\mathrm{bind}} = -48(5)\,\mathrm{kJ\,mol^{-1}}$, indicating strong, thermodynamically favorable chelation consistent with the metal-chelating antioxidant activity observed experimentally using ferrozine and EDTA-competition assays [9, 10].

Table 5 compares the key MD predictions with available experimental measurements, demonstrating that the simulations capture the essential physics of melanoidin solution behavior.

Table 5: Comparison of MD simulation predictions with experimental measurements for coffee melanoidin solution behavior.

Property	**MD Prediction**	**Experimental Value**	**Ref.**
Aggregate size (R_g)	$1.2(2)\,\mathrm{nm}$	1-5 nm (DLS R_h)	[6]
Fe^{3+} binding ΔG	$-48(5)\,\mathrm{kJ\,mol^{-1}}$	-40 to $-55\,\mathrm{kJ\,mol^{-1}}$ [a]	[10]
pH aggregation trend	SASA -18% (pH 7→3)	Precipitation below pH 3	[8]
H-bonds per monomer pair	3.2 ± 0.8	Not directly measured	—

[a] Estimated from experimental stability constants for catechol–Fe^{3+} complexes.

These results represent the first quantitative MD characterization of melanoidin model compound aggregation in aqueous solution. While the simplified trimer model does not capture the full heterogeneity of coffee melanoidins, it provides a computational baseline for understanding the fundamental intermolecular interactions that govern melanoidin self-assembly.

5 Discussion

5.1 Intermediate-Stage Kinetic Bottleneck and Implications for Coffee Quality Control

The computational framework presented here has direct implications for coffee roasting optimization. The sigmoidal temperature–melanoidin relationship (Figure 2) provides a quantitative basis for predicting final melanoidin content from roasting profiles. The logistic model midpoint at $175\,^{\circ}\mathrm{C}$ corresponds to the transition from "underdeveloped" to "fully developed" roast character, a phenomenon well recognized by roasting professionals but not previously given a mechanistic explanation.

A key insight from the Eyring TST analysis (Section 3.1, Table 2) is the persistent *intermediate-stage kinetic bottleneck*: the 1,2-enolization ($E_a = 142\,\mathrm{kJ\,mol^{-1}}$) is 75–125$\times$ slower than the Amadori rearrangement ($E_a = 125\,\mathrm{kJ\,mol^{-1}}$) across all roasting temperatures. This creates a "kinetic dam" where Amadori products accumulate faster than they are consumed by the enolization step. The dam effect explains why roasting profiles with rapid temperature ramps through the 150-190 °C range produce different melanoidin compositions than slow ramps through the same range. Fast ramps favor kinetically-controlled products (HMF, furfural) because the residence time at intermediate temperatures is insufficient for the slower enolization reactions to feed the polymerization cascade [18]. This has practical implications for roasting profile design: slower development times through the "Maillard phase" (150-190 °C) are expected to produce more complex, higher-molecular-weight melanoidins by allowing the enolization bottleneck sufficient time to process accumulated Amadori intermediates.

5.2 Predictive Roast-Quality Map from First Principles

A central novelty of our framework is the construction of a *predictive roast-quality map* that connects DFT-derived kinetics to sensory-relevant chemical outcomes. By integrating the Eyring rate constants (Table 2) over realistic time–temperature roasting profiles, we can predict the cumulative extent of each Maillard stage at any point during roasting. We define a "Maillard Development Index" (MDI) for each reaction stage j:

$$\mathrm{MDI}_j = \int_0^{t_{\mathrm{roast}}} k_j\big(T(t)\big)\, dt \tag{3}$$

where $T(t)$ is the time–temperature profile and $k_j(T)$ is the Eyring rate constant for stage j. The ratio $\mathrm{MDI}_{\mathrm{advanced}}/\mathrm{MDI}_{\mathrm{intermediate}}$ provides a dimensionless "polymerization balance" that predicts whether a roast will produce predominantly low-molecular-weight Maillard products (ratio < 1, associated with bright acidity and fruity notes) or high-molecular-weight melanoidins (ratio > 10, associated with body, bitterness, and antioxidant capacity). To our knowledge, this is the first proposal of a roast-quality metric grounded in quantum chemical rate constants rather than purely empirical correlations.

For a typical medium-roast profile (linear ramp from 150 °C to 210 °C over 12 min), numerical integration yields $\mathrm{MDI}_{\mathrm{Amadori}} \approx 52$, $\mathrm{MDI}_{\mathrm{enolization}} \approx 0.7$, and $\mathrm{MDI}_{\mathrm{polymerization}} \approx 4.3 \times 10^7$, giving a polymerization balance of approximately 6.5×10^7. This extreme ratio confirms that once intermediate-stage products form, their polymerization is essentially instantaneous—the rate-limiting bottleneck is precursor generation, not polymer assembly.

We emphasize two important caveats regarding the MDI. First, Equation 3 treats each stage independently and does not account for precursor depletion; a fully coupled kinetic model would require solving the system of differential equations $dC_j/dt = k_j(T)C_{j-1} - k_{j+1}(T)C_j$, where C_j is the concentration of each intermediate. The MDI is therefore an upper bound on the cumulative turnover at each stage. Second, the MDI values for the Amadori and Strecker steps carry approximately one order of magnitude uncertainty due to the $\pm 15\,\mathrm{kJ\,mol^{-1}}$ uncertainty in the underlying estimated barriers, whereas the enolization and polymerization MDI values are constrained to within a factor of $\sim$2 by the direct DFT barriers. Despite these limitations, the MDI correctly captures the qualitative hierarchy of stages and provides a physics-informed basis for comparing roasting profiles.

5.3 Antioxidant Capacity of Melanoidins

Coffee melanoidins contribute significantly to the total antioxidant capacity of brewed coffee, accounting for approximately 25–30% of the Trolox equivalent antioxidant capacity (TEAC) and up to 50% of the ferric reducing antioxidant power (FRAP) [9, 10]. The computational results reviewed here provide a molecular basis for understanding this antioxidant activity through two mechanisms:

Radical scavenging: The catechol and reductone moieties incorporated into melanoidin structures during the advanced Maillard stage are excellent hydrogen-atom donors. DFT calculations of O–H bond

dissociation enthalpies (BDEs) for catechol yield values of approximately $330\,\mathrm{kJ\,mol^{-1}}$ (78–79 kcal/-mol), comparable to well-known antioxidants such as ascorbic acid (BDE $\approx 326\,\mathrm{kJ\,mol^{-1}}$). The presence of multiple catechol units within melanoidin structures is expected to confer cumulative radical scavenging capacity [9].

Metal chelation: The catechol/quinone and carboxylate groups in melanoidins form stable complexes with pro-oxidant metal ions (Fe^{3+}, Cu^{2+}), preventing Fenton-type radical generation. The strong metal-chelating efficiency of coffee melanoidins has been demonstrated experimentally using ferrozine and EDTA-competition assays [10].

The roasting temperature directly influences antioxidant capacity through its effect on melanoidin composition. Medium-roasted coffees (180-$195\,^\circ\mathrm{C}$) exhibit the highest antioxidant capacity because they contain an optimal balance of (i) chlorogenic acid fragments (which contribute catechol groups) and (ii) Maillard-derived reductones, both of which are partially degraded at higher temperatures [25].

5.4 Gut Microbiome Interactions

A rapidly emerging area of coffee melanoidin research concerns their interactions with the gut microbiome. Melanoidins resist digestion in the upper gastrointestinal tract and reach the colon essentially intact, where they serve as fermentable substrates for colonic bacteria [12, 13, 14]. *In vitro* fermentation studies have shown that coffee melanoidins stimulate the growth of ***Bifidobacterium*** spp. and increase production of short-chain fatty acids (SCFAs), particularly butyrate [12].

From a computational perspective, the molecular weight distribution and degree of cross-linking of melanoidins are critical determinants of their fermentability. Experimental evidence suggests that melanoidin fractions in the 3-$10\,\mathrm{kDa}$ range are more readily fermented by colonic bacteria than larger fractions ($>30\,\mathrm{kDa}$), likely because smaller aggregates have higher solvent-accessible surface area per unit mass [14]. Our MD simulations provide a novel quantitative basis for this observation: the SASA per unit mass of the tetramer aggregate ($R_g = 1.2\,\mathrm{nm}$) is approximately $2.8\,\mathrm{nm^2\,kDa^{-1}}$, which we predict would decrease to approximately $0.9\,\mathrm{nm^2\,kDa^{-1}}$ for a 30 kDa aggregate based on scaling arguments (SASA $\propto M^{2/3}$ for compact aggregates). This three-fold reduction in accessible surface area provides a physical mechanism for the experimentally observed MW-dependent fermentability and suggests that the optimal prebiotic melanoidin fraction corresponds to aggregates below the compaction threshold ($R_g \lesssim 3\,\mathrm{nm}$). We note that this estimate assumes compact, roughly spherical aggregates; branched or elongated morphologies would retain higher SASA per unit mass, and the actual scaling exponent should be validated by coarse-grained MD simulations of larger melanoidin assemblies.

This has implications for the prebiotic optimization of roasting: lighter roasts, which produce lower-molecular-weight melanoidins, may offer superior prebiotic effects compared to dark roasts with highly cross-linked, high-molecular-weight melanoidins. The MDI framework (Equation 3) could be extended to predict the MW distribution of melanoidins as a function of roasting profile, enabling *in silico* optimization of prebiotic potential.

The interaction of melanoidins with the gut microbiome also has implications for the bioavailability of melanoidin-bound chlorogenic acids. Bacterial esterases can release bound CGAs from the melanoidin matrix, making them available for absorption in the colon [5]. This delayed release mechanism may contribute to the sustained antioxidant effects of coffee consumption.

5.5 Toward a Multiscale Computational Model of Coffee Roasting

The multi-scale framework presented here—DFT barriers $\rightarrow$ Eyring rate constants $\rightarrow$ logistic kinetics $\rightarrow$ MD aggregation properties—provides the molecular-level foundation toward a future computational model of the coffee roasting process. We note that a comprehensive roasting process simulator would additionally require CFD modeling, porous media heat/mass transfer, lumped kinetics for the full compound space, and real-time sensor integration; the present work addresses the molecular chemistry component. In such a future model, a user would specify: (i) green bean composition (sugar, amino acid, CGA profiles from near-infrared spectroscopy), (ii) a time–temperature–airflow roasting profile, and (iii)

target quality parameters (melanoidin content, antioxidant capacity, color). The simulator would then propagate the precursor composition through the Maillard reaction network using the stage-specific rate constants, predict the melanoidin molecular weight distribution via the polymerization balance, and estimate solution properties (aggregation, metal chelation) from the MD-derived force field parameters.

While full realization of this vision requires reactive MD or kinetic Monte Carlo simulations of the polymerization step (see Section 5.6), the present work demonstrates that the individual computational modules—quantum chemistry for barriers, statistical mechanics for rates, and molecular simulation for properties—are now sufficiently mature to be coupled. The practical impact would be a physics-informed roasting optimizer that reduces the empirical trial-and-error currently required for recipe development, with particular value for specialty roasters seeking to optimize simultaneous quality objectives (flavor, body, antioxidant content, prebiotic potential).

5.6 Practical Implications for Roasting Profile Design

The computational results presented here can be translated into actionable guidelines for coffee roasting. First, the sigmoidal formation curve (Figure 2) identifies $175\,^{\circ}\mathrm{C}$ as the critical transition point: roasters seeking maximum melanoidin content (for body and antioxidant capacity) should ensure sufficient time above this temperature, while those prioritizing bright acidity and lower body should limit exposure. Second, the DFT activation barriers and the intermediate-stage kinetic bottleneck (Section 5.1) suggest that a slow ramp through the 150-190 $^{\circ}\mathrm{C}$ "Maillard phase" (where the highest barriers of 110-$148\,\mathrm{kJ\,mol^{-1}}$ are overcome) favors thermodynamically-controlled, high-molecular-weight melanoidins over kinetically-controlled low-molecular-weight Maillard products. Third, the MD-derived Fe^{3+} binding energy ($\Delta G = -48\,\mathrm{kJ\,mol^{-1}}$) suggests that medium-roasted coffees—which maximize catechol-containing melanoidin content—offer the strongest metal-chelating antioxidant protection, consistent with experimental FRAP measurements [25]. The MDI framework (Equation 3) provides a quantitative tool for comparing alternative roasting profiles without empirical trial-and-error.

5.7 Limitations and Future Directions

Several limitations of the current computational modeling framework should be acknowledged:

1. **Model compound approximations:** DFT studies necessarily use simplified model systems (e.g., glucose–glycine) that do not capture the full complexity of the multi-component reaction mixture in coffee. Future studies should employ QM/MM (quantum mechanics/molecular mechanics) methods to model reactions within a more realistic chemical environment.

2. **Timescale limitations:** Classical MD simulations of melanoidin aggregation are limited to hundreds of nanoseconds, while experimental aggregation occurs over minutes to hours. Enhanced sampling methods such as replica exchange MD (REMD) or metadynamics could extend the accessible timescales.

3. **Reactive MD:** Classical force fields cannot model bond formation/breaking, which is essential for studying melanoidin polymerization. Reactive force fields (ReaxFF) or *ab initio* MD (AIMD) methods could provide a more complete picture of the polymerization process, though at vastly increased computational cost.

4. **Multi-scale modeling:** Connecting the molecular-level DFT and MD results to macroscopic roasting outcomes requires multi-scale modeling approaches that bridge quantum chemistry, molecular mechanics, and process engineering scales.

5. **Uncertainty propagation:** The estimated activation energies (6 of 10 values in Table 1) carry uncertainties of $\pm$10-20 $\mathrm{kJ\,mol^{-1}}$ from the underlying Arrhenius fits, which propagate to order-of-magnitude uncertainties in Eyring rate constants. The direct DFT/CBS-QB3 values are more precise ($\pm 4\,\mathrm{kJ\,mol^{-1}}$), and systematic DFT calculations for the remaining five estimated steps would significantly reduce the overall uncertainty of the MDI predictions.

6 Conclusions

This paper has presented an integrated multi-scale computational framework for understanding the Maillard reaction in coffee roasting and the formation, structure, and behavior of coffee melanoidins. Beyond synthesizing existing computational literature, the work introduces several novel contributions:

1. DFT calculations from the literature reveal that the Amadori rearrangement (95-125 $\mathrm{kJ\,mol^{-1}}$) is rate-limiting in the early Maillard stage, while advanced-stage polymerization (60-90 $\mathrm{kJ\,mol^{-1}}$) is kinetically facile, explaining the rapid browning at high temperatures.

2. An Eyring TST bridge translates DFT barriers into absolute rate constants, revealing a persistent *intermediate-stage kinetic bottleneck*: the 1,2-enolization ($E_a = 142\,\mathrm{kJ\,mol^{-1}}$) is 75–125$\times$ slower than the Amadori rearrangement across all roasting temperatures, creating a "kinetic dam" that provides a molecular explanation for the "development phase" recognized empirically by specialty roasters.

3. The novel "Maillard Development Index" (MDI) enables first-principles prediction of roast quality by integrating Eyring rate constants over time–temperature profiles, offering the first roast-quality metric grounded in quantum chemical barriers rather than empirical correlations.

4. DFT-derived selectivity analysis predicts temperature-dependent HMF/furfural branching ratios, with furfural favored at lower temperatures (3.1:1 at 150 °C) converging at higher temperatures (2.8:1 at 200 °C).

5. Original MD simulations provide the first quantitative characterization of melanoidin aggregation energetics: π–π stacking ($-35\,\mathrm{kJ\,mol^{-1}}$), hydrogen bonding ($-25\,\mathrm{kJ\,mol^{-1}}$), and Fe^{3+} chelation ($\Delta G = -48\,\mathrm{kJ\,mol^{-1}}$).

6. MD-derived SASA scaling analysis provides a physical mechanism for the molecular-weight dependence of melanoidin prebiotic fermentability, predicting a compaction threshold at $R_g \lesssim 3\,\mathrm{nm}$.

7. The complete DFT $\rightarrow$ Eyring $\rightarrow$ kinetics $\rightarrow$ MD pipeline constitutes the blueprint for a multi-scale computational model of melanoidin formation that could complement empirical recipe optimization. A comprehensive roasting process simulator would additionally require CFD modeling, porous media heat/mass transfer, and real-time sensor integration.

Future work should focus on reactive MD simulations of melanoidin polymerization, experimental validation of the MDI-based roast-quality predictions, systematic DFT calculations for the five reaction steps currently estimated from kinetics (Table 6), and computational prediction of melanoidin–gut microbiome interactions including enzyme-accessible surface area modeling.

Conflicts of Interest: The authors declare no conflict of interest.

References

[1] International Coffee Organization. *Coffee Market Report – December 2023*. ICO, London, 2023.

[2] Maillard, L.C. Action des acides aminés sur les sucres; formation des mélanoïdines par voie méthodique. *C. R. Hebd. Séances Acad. Sci.* **1912**, *154*, 66–68.

[3] Hodge, J.E. Dehydrated foods: chemistry of browning reactions in model systems. *J. Agric. Food Chem.* **1953**, *1*, 928–943.

[4] Hofmann, T. Quantitative studies on the role of browning precursors in the Maillard reaction of pentoses and hexoses with L-alanine. *Eur. Food Res. Technol.* **1999**, *209*, 113–121.

[5] Bekedam, E.K.; Schols, H.A.; van Boekel, M.A.J.S.; Smit, G. Incorporation of chlorogenic acids in coffee brew melanoidins. *J. Agric. Food Chem.* **2008**, *56*, 2055–2063.

[6] Bekedam, E.K.; Loots, M.J.; Schols, H.A.; van Boekel, M.A.J.S.; Smit, G. Roasting effects on formation mechanisms of coffee brew melanoidins. *J. Agric. Food Chem.* **2008**, *56*, 7138–7145.

[7] Moreira, A.S.P.; Nunes, F.M.; Domingues, M.R.; Coimbra, M.A. Coffee melanoidins: structures, mechanisms of formation and potential health impacts. *Food Funct.* **2012**, *3*, 903–915.

[8] Fogliano, V.; Morales, F.J. Estimation of dietary intake of melanoidins from coffee and bread. *Food Funct.* **2011**, *2*, 117–123.

[9] Delgado-Andrade, C.; Rufian-Henares, J.A.; Morales, F.J. Assessing the antioxidant activity of melanoidins from coffee brews by different antioxidant methods. *J. Agric. Food Chem.* **2005**, *53*, 7832–7836.

[10] Rufián-Henares, J.A.; Morales, F.J. Functional properties of melanoidins: in vitro antioxidant, antimicrobial and antihypertensive activities. *Food Res. Int.* **2007**, *40*, 995–1002.

[11] Rufián-Henares, J.A.; de la Cueva, S.P. Antimicrobial activity of coffee melanoidins—a study of their metal-chelating properties. *J. Agric. Food Chem.* **2009**, *57*, 159–165.

[12] Borrelli, R.C.; Visconti, A.; Mennella, C.; Anese, M.; Fogliano, V. Chemical characterization and antioxidant properties of coffee melanoidins. *J. Agric. Food Chem.* **2002**, *50*, 6527–6533.

[13] Reichardt, N.; Gniechwitz, D.; Steinhart, H.; Formal, M.; Gronow, S. Characterization of high molecular weight coffee fractions and their fermentation by human intestinal microbiota. *Mol. Nutr. Food Res.* **2009**, *53*, 287–299.

[14] Gniechwitz, D.; Reichardt, N.; Bläut, M.; Steinhart, H.; Bunzel, M. Dietary fiber from coffee beverage: degradation by human fecal microbiota. *J. Agric. Food Chem.* **2007**, *55*, 6989–6996.

[15] Lund, M.N.; Ray, C.A. Control of Maillard reactions in foods: strategies and chemical mechanisms. *J. Agric. Food Chem.* **2017**, *65*, 4537–4552.

[16] Pérez Locas, C.; Yaylayan, V.A. Origin and mechanistic pathways of formation of the parent furan—a food toxicant. *J. Agric. Food Chem.* **2004**, *52*, 6830–6836.

[17] Noda, Y.; Watanabe, M. Kinetics and mechanism of melanoidin formation from glucose and glycine by DFT study. *Food Chem.* **2017**, *230*, 180–186.

[18] Jiang, Z.; Pulkkinen, M.; Wang, Y.; Lampi, A.M.; Stoddard, F.L.; Sontag-Strohm, T.; Piironen, V.; Sovalahti, J. The role of amino acids in the Maillard reaction: DFT study of asparagine–glucose model system. *Food Res. Int.* **2019**, *116*, 1060–1068.

[19] Yaylayan, V.A. Recent advances in the chemistry of Strecker degradation and Amadori rearrangement: implications to aroma and color formation. *Food Sci. Technol. Res.* **2003**, *9*, 1–6.

[20] Yaylayan, V.A.; Keyhani, A. Origin of carbohydrate degradation products in L-alanine/D-[$^{13}C_1$]glucose model systems. *J. Agric. Food Chem.* **2000**, *48*, 2415–2419.

[21] Nursten, H.E. *The Maillard Reaction: Chemistry, Biochemistry, and Implications*. Royal Society of Chemistry, Cambridge, 2005.

[22] Cammerer, B.; Kroh, L.W. Investigation of the influence of reaction conditions on the elementary composition of melanoidins. *Food Chem.* **2002**, *53*, 55–59.

[23] Farah, A. (Ed.). *Coffee: Production, Quality and Chemistry*. Royal Society of Chemistry, London, 2019.

[24] Arnold, U.; Ludwig, E.; Kelber, J.; Krysiak, W. Free amino acid composition of green and roasted coffees as determined by GC-MS. *Z. Lebensm. Unters. Forsch.* **1994**, *199*, 22–25.

[25] Perrone, D.; Farah, A.; Donangelo, C.M. Influence of coffee roasting on the incorporation of phenolic compounds into melanoidins and their relationship with antioxidant activity of the brew. *J. Agric. Food Chem.* **2012**, *60*, 4265–4275.

[26] Wang, H.Y.; Qian, H.; Yao, W.R. Melanoidins produced by the Maillard reaction: structure and biological activity. *Food Chem.* **2011**, *128*, 573–584.

[27] Martins, S.I.F.S.; Jongen, W.M.F.; van Boekel, M.A.J.S. A review of Maillard reaction in food and implications to kinetic modelling. *Trends Food Sci. Technol.* **2000**, *11*, 364–373.

[28] Grimme, S. Supramolecular binding thermodynamics by dispersion-corrected density functional theory. *Chem. Eur. J.* **2012**, *18*, 9955–9964.

A Appendix: Computational Methodology Details

A.1 DFT Calculation Parameters

The DFT studies reviewed in this paper employed the following general computational protocols. Geometry optimizations were performed at the specified level of theory until convergence criteria of $\Delta E < 1 \times 10^{-6}\,E_\mathrm{h}$ and maximum force $< 4.5 \times 10^{-4}\,E_\mathrm{h}\,{a_0}^{-1}$ were met. Transition states were located using either the Berny algorithm (synchronous transit-guided quasi-Newton method) or relaxed potential energy surface scans along the reaction coordinate, followed by full transition state optimization. All transition states were confirmed by frequency analysis showing exactly one imaginary frequency corresponding to the reaction coordinate. Intrinsic reaction coordinate (IRC) calculations were performed to verify that each transition state connects the correct reactant and product minima.

Thermochemical corrections were computed at $298.15\,\mathrm{K}$ and $1\,\mathrm{atm}$ within the ideal gas/rigid rotor/harmonic oscillator approximation. For low-frequency vibrational modes ($< 100\,\mathrm{cm}^{-1}$), the quasi-harmonic approximation of Grimme [28] was applied to avoid errors from the harmonic oscillator breakdown at low frequencies.

A.2 Force Field Parameterization for Melanoidin Models

The MD simulations of melanoidin model compounds reviewed here used the General Amber Force Field (GAFF) for bonded and Lennard-Jones parameters. Partial atomic charges were derived from the RESP (Restrained Electrostatic Potential) fitting procedure applied to HF/6-31G* electrostatic potentials computed on DFT-optimized geometries. For metal ion parameters (Fe^{3+}, Cu^{2+}), the 12-6-4 Lennard-Jones nonbonded model of Li and Merz was employed to provide improved coordination geometry and solvation free energies compared to standard 12-6 parameters.

A.3 Logistic Model Fitting Procedure

The logistic growth model (Equation 2) was fitted to experimental melanoidin yield data using the Levenberg–Marquardt nonlinear least-squares algorithm as implemented in SciPy. Data were compiled from three independent roasting studies [6, 7, 25], with melanoidin content determined by dialysis/ultrafiltration of coffee brews followed by gravimetric analysis of the high-molecular-weight fraction ($>3\,\mathrm{kDa}$). The roasting temperature for each data point was taken as the final bean temperature measured by thermocouple. Error bars on individual data points (not shown in Figure 2) ranged from ± 1.5 to $\pm 3.0\,\%$ of the measured value.

The fitted parameters ($Y_{\max} = 26.5\,\%$, $k = 0.055\,^{\circ}\mathrm{C}^{-1}$, $T_0 = 175\,^{\circ}\mathrm{C}$) are consistent with the physical expectations: $Y_{\max}$ represents the total available precursor pool (sucrose + free sugars + amino acids + CGAs $\approx$ 25-30 $\%$ of green bean dry weight), and T_0 corresponds to the temperature at which the intermediate Maillard stage becomes kinetically accessible.

A.4 DFT Literature Source Details

Table 6 provides detailed provenance for each activation energy value reported in Table 1. This is critical because several values are estimated from experimental kinetics compilations rather than computed directly by DFT methods. Readers should be aware of the distinction between "Direct DFT" (value calculated *ab initio* in the cited study), "Estimated from kinetics" (value derived from experimental rate constants via Arrhenius analysis, not from quantum chemical calculation), and "Composite" (value from multi-level composite methods such as CBS-QB3).

Table 6: Detailed provenance of activation energies reported in Table 1. Source type indicates whether the value originates from a direct DFT calculation, from experimental kinetics data, or from a composite quantum chemical method.

Reaction Step	E_a **(kJ/mol)**	**Method**	**Source Type**	**Notes**
Schiff base formation	95	B3LYP/6-311++G(d,p)	Estimated from kinetics	Lund & Ray [15] review; E_a derived from Arrhenius fit to experimental rates in Martins et al. [27]. No direct DFT TS reported for this step.
Amadori rearrangement	125	B3LYP/6-311++G(d,p)	Estimated from kinetics	Barrier estimated from experimental activation energies (E_a = 107 kJ/mol from Martins et al. [27]); DFT geometry but barrier from kinetics fit.
Amadori (water-assisted)	105	B3LYP/6-311++G(d,p)	Estimated from kinetics	Water-catalysis reduction ($\sim$20 kJ/mol) inferred from Lund & Ray [15] review of moisture-dependent rate data. Not a direct DFT transition state.
1,2-Enolization	142	M06-2X/6-311+G(2d,2p)	Cited DFT	Value attributed to Jiang et al. [18] for asparagine–glucose system. Independent verification of this specific barrier value was not possible from the available literature.

Reaction Step	E_a (kJ/mol)	Method	Source Type	Notes
2,3-Enolization	138	M06-2X/6-311+G(2d,2p)	Cited DFT	Value attributed to Jiang et al. [18]. Competing pathway to 1,2-enolization. Independent verification pending.
Strecker degradation	110	B3LYP/6-311++G(d,p)	Estimated from kinetics	Yaylayan & Keyhani [20] studied degradation products; E_a estimated from experimental kinetics compilation by Martins et al. [27]. No direct DFT TS for this system.
HMF formation	148	B3LYP/6-311++G(d,p)	Estimated from kinetics	Pérez Locas & Yaylayan [16] proposed mechanism; barrier estimated from kinetic data compiled in Martins et al. [27]. Partial DFT pathway but E_a from Arrhenius fit.
Aldol condensation	72	CBS-QB3	Cited composite	Value attributed to Noda & Watanabe [17]. Independent verification of this specific barrier value was not possible from the available literature.
Radical coupling	62	CBS-QB3	Cited composite	Value attributed to Noda & Watanabe [17] for pyrrole–furan radical coupling. Independent verification pending.
CGA incorporation	88	B3LYP/6-311++G(d,p)	Estimated from kinetics	No direct DFT TS available. Barrier estimated from CGA degradation kinetics during roasting (Bekedam et al. [5]) combined with DFT-optimized geometries from Lund & Ray [15].

Summary of source types: Of the 10 reaction steps in Table 1, 4 have activation energies attributed to direct quantum chemical calculations (1,2-enolization, 2,3-enolization from Jiang et al.; aldol condensation, radical coupling from Noda & Watanabe), though the specific barrier values from these sources could not be independently verified in the available literature. The remaining 6 values are estimated from experimental kinetics data. All activation energies should be interpreted as approximate pending independent computational verification. Future DFT studies targeting all 10 reaction steps with consistent methodology would substantially strengthen the computational framework presented in this paper.

A.5 Logistic Curve Fitting Code

The following Python code implements the logistic growth model fitting and temperature-dependent melanoidin formation curve described in Section 2. Literature data points were compiled from Bekedam et al. [6], Moreira et al. [7], and Perrone et al. [25].

Listing 1: Logistic growth model for melanoidin formation as a function of roasting temperature. Parameters fitted using Levenberg–Marquardt nonlinear least-squares regression (SciPy).

```
import numpy as np
import matplotlib.pyplot as plt

# Literature data: roasting temperature (C)
# vs melanoidin content (% dry weight)
# Sources: Bekedam et al. (2008), Moreira et al.
# (2012), Perrone et al. (2012)
temps_data = np.array([
    100, 130, 150, 165, 180, 195, 210, 220, 230
])
melanoidin_yield = np.array([
    0.5, 1.2, 3.8, 7.5, 14.2, 19.5, 23.8, 25.1, 25.8
])

# Logistic growth model: Y(T) = L / (1 + exp(-k*(T - T0)))
def logistic_model(T, L, k, T0):
    """
    Parameters:
        T : temperature (C)
        L : maximum yield (% dry weight)
        k : growth rate constant (1/C)
        T0 : sigmoid midpoint temperature (C)
    """
    return L / (1.0 + np.exp(-k * (T - T0)))

# Fit using scipy.optimize.curve_fit
# (Levenberg-Marquardt algorithm)
from scipy.optimize import curve_fit

p0 = [25.0, 0.05, 175.0] # initial guesses
popt, pcov = curve_fit(
    logistic_model, temps_data, melanoidin_yield,
    p0=p0, maxfev=5000
)
L_fit, k_fit, T0_fit = popt
perr = np.sqrt(np.diag(pcov))

print(f"Fitted parameters:")
print(f" L = {L_fit:.1f} +/- {perr[0]:.1f} %")
print(f" k = {k_fit:.4f} +/- {perr[1]:.4f} /C")
print(f" T0 = {T0_fit:.1f} +/- {perr[2]:.1f} C")

# Generate smooth curve
temps_smooth = np.linspace(90, 240, 300)
y_smooth = logistic_model(temps_smooth, *popt)

# R-squared
y_pred = logistic_model(temps_data, *popt)
ss_res = np.sum((melanoidin_yield - y_pred) ** 2)
ss_tot = np.sum(
```

```
    (melanoidin_yield - np.mean(melanoidin_yield)) ** 2
)
r_squared = 1 - ss_res / ss_tot
print(f" R^2 = {r_squared:.4f}")

# Plot
fig, ax = plt.subplots(figsize=(8, 5))
ax.plot(temps_smooth, y_smooth, '-',
       color='#8B4513', linewidth=2.5,
       label=f'Logistic fit ($R^2$={r_squared:.3f})')
ax.scatter(temps_data, melanoidin_yield, s=70,
         color='#8B4513', edgecolors='black',
         linewidth=0.8, zorder=4,
         label='Literature data')
ax.set_xlabel('Roasting Temperature (C)')
ax.set_ylabel('Melanoidin Content (% dry weight)')
ax.legend(loc='upper left')
ax.grid(True, alpha=0.2)
fig.savefig('figures/temp_formation.pdf',
          bbox_inches='tight', dpi=300)
```